13th International Symposium on Particle Image Velocimetry – ISPIV 2019
Munich, Germany, July 22-24, 2019

Aerodynamic pressure reconstruction on generic surfaces from robotic PIV measurements

Constantin Jux[1]*, Andrea Sciacchitano[1], Fulvio Scarano[1]

[1]Delft University of Technology, Department of Aerospace Engineering – Aerodynamics
Delft, The Netherlands

*C.Jux@tudelft.nl

Abstract

A multi-model method for static pressure evaluations based on 3D PTV data is presented. The volumetric measurement domain is partitioned into an irrotational part where pressure is evaluated in a point-wise manner through Bernoulli's equation, and a rotational domain where the pressure gradient is spatially integrated. In a third step, the field pressure is mapped onto the solid surface of the object. The method is first assessed on the flow around a 15 cm diameter sphere at 10 m/s. A good agreement is observed for the surface pressure prior to flow separation. Discrepancies in the order of 0.1 to 0.2 C_p are found towards the separated wake region. There is little dependency on spatial resolution, as long as the ensemble averaging cell remains below 50% of the local radius of curvature of the object. The potential of the method to address generic three-dimensional problems of higher geometrical complexity is demonstrated for the time-averaged flow field around a full-scale cyclist, within a 2 m^3 measurement domain. The proposed combination of the multi-model pressure evaluation with robotic PIV enables surface pressure measurements in the low-speed flow regime, for unprecedented aerodynamic analysis otherwise possible only by massive instrumentation of the test model with surface pressure taps.

1 Introduction

Surface pressure measurements are crucial to determine the distribution of the aerodynamic loads on a wind tunnel model. Accurate measurements are typically obtained by probing the model with a multitude of static pressure taps, see e.g. Tropea et al. (2007). In industrial tests, the number of wall taps rapidly grows to hundreds or thousands, increasing design complexity and costs of such models, while a-priori knowledge on the flow topology is necessary for a smart placement of the pressure orifices. In high-speed applications, the use of pressure sensitive paint (PSP) provides a suitable alternative (Gregory et al., 2008). However, its limited sensitivity in low-speed applications prevents extensive utilization of this technique, see e.g. Tagliabue et al. (2017). Evaluating the aerodynamic pressure from particle image velocimetry (PIV) data has become more feasible in recent years, as can be seen in the topical review by van Oudheusden (2013). It is worthwhile noting that within this field much attention has been devoted, in particular in the domain of aeroacoustics, towards the measurement of unsteady pressure fluctuations by means of PIV (see e.g. Ghaemi et al., 2012; Pröbsting et al., 2013; Huhn et al., 2018; among others). Instead, the relatively simple problem of the time-averaged surface pressure has been seldom looked at, despite being of much relevance for the analysis of aerodynamic performance.

Evaluating pressure distributions on industrial-scale and generic geometries requires volumetric PIV techniques with sufficient optical access. These characteristics are found in coaxial volumetric velocimetry (CVV, Schneiders et al., 2018) and its application in robotic volumetric PIV (Jux et al., 2018a). In a previous work of the authors (Jux et al., 2018b), the latter technique is applied to evaluate the surface pressure distribution of a sphere. The wall pressure was determined by linear extrapolation of the flow field pressure obtained through the commonly applied Poisson approach

(de Kat and van Oudheusden 2012). It was noticed that the large experimental errors close to the fluid-solid interface (light reflections and under-resolved velocity gradient) compromises the results over wider regions of the measurement domain. To this end, an alternative multi-model-approach to evaluate the static pressure on generic surfaces is investigated in this work, yielding a more robust reconstruction of the surface pressure distribution.

The proposed technique relies on the partition of the measurement domain into a rotational and an irrotational flow region. In many practical situations, large portions of the flow domain are irrotational and as such, full integration of the Poisson equation with the associated error propagation, is not needed. Instead, the pressure in the former region can be modeled through potential flow theory (Bernoulli equation), restricting the region where spatial integration of the pressure gradient is required to a smaller region between the latter and the solid surface of the object. A third, yet crucial step is that of interfacing the data discretization in the flow domain (typically Cartesian) with the surface discretization where the pressure is mapped.

The working principles of the developed method are outlined in Sec. 2, and its performance is assessed on the flow past a 15 cm diameter sphere at 10 m/s (Re_d = 10^5), where static pressure taps serve as a reference measurement for the pressure distribution. Details of the experimental apparatus are shown in Sec. 3, followed by a discussion of the results in Sec. 4. Subsequently, the potential of the technique is exposed by its application to the flow around a full-scale cyclist mannequin.

2 Methodology

The focus of this work is the evaluation of the time-averaged surface pressure based on 3D PTV data. The key procedures of the velocity field measurement by robotic PIV are summarized in Sec. 2.1. The pressure evaluation approach and the method to infer the pressure distribution from the flow field to the model surface is featured in Sec. 2.2. This is followed by a discussion of the domain identification in Sec. 2.3, which defines the boundary between rotational and irrotational flow.

2.1 Velocity field measurement by robotic PIV

In this work, 3D PTV measurements carried out by the robotic volumetric PIV technique (Jux et al., 2018a) are considered. Particle images are acquired by a coaxial volumetric velocimetry (CVV) probe, which may be characterised as a low-aperture tomographic imaging system. The measurement uncertainty along the coaxial imaging direction is higher as compared to the in-plane components. Yet, the overall measurement uncertainty is improved by means of track-based regularization as discussed in Schneiders et al. (2018). This can be done since time-resolved images are acquired and Lagrangian Particle Tracking (LPT, Shake-The-Box (STB), Schanz et al., 2016) is used to identify and follow the tracers. The CVV system is positioned and manipulated by a robotic arm, allowing for the scanning of large measurement volumes. Finally, the sparse and randomly distributed instantaneous velocity data is spatially and temporally averaged by means of ensemble averaging, resulting in a time-averaged velocity field on a uniform Cartesian grid, also referred to as the *fluid mesh*. In this work, the velocity inside each cell (also referred to as a bin) is modelled by a first order polynomial in 3D fitted to the LPT data, following the work of Agüera et al. (2015),

$$\overline{\boldsymbol{u}}(\boldsymbol{x}) = \boldsymbol{a}_0 + \boldsymbol{a}_1 x + \boldsymbol{a}_2 y + \boldsymbol{a}_3 z \tag{1}$$

The above provides an estimate for the mean velocity $\overline{\boldsymbol{u}}$ and its gradient. Moreover, the approach allows for an improved estimation of the unsteady components u' as compared to averaging methods not accounting for the spatial variation of the velocity inside the bin. The measurement of the fluctuating terms is relevant in the accurate computation of the time-averaged pressure gradient, which includes the spatial gradient of the Reynolds stress tensor.

2.2 Pressure calculation

The static pressure in the measurement domain and on the object surface is evaluated in a multi-model approach. Conventional pressure evaluation methods, such as the Poisson approach and spatial integration methods, can be prone to error accumulation over lengthy integration path and

inaccurate specification of boundary conditions on curved geometries. This is illustrated by the example of a 2D cylinder flow in Fig. 1 (left), where one would apply Neumann type boundary conditions downstream of the object and on the object surface itself, while using a Dirichlet type specification on the remaining boundaries where freestream conditions may be assumed.

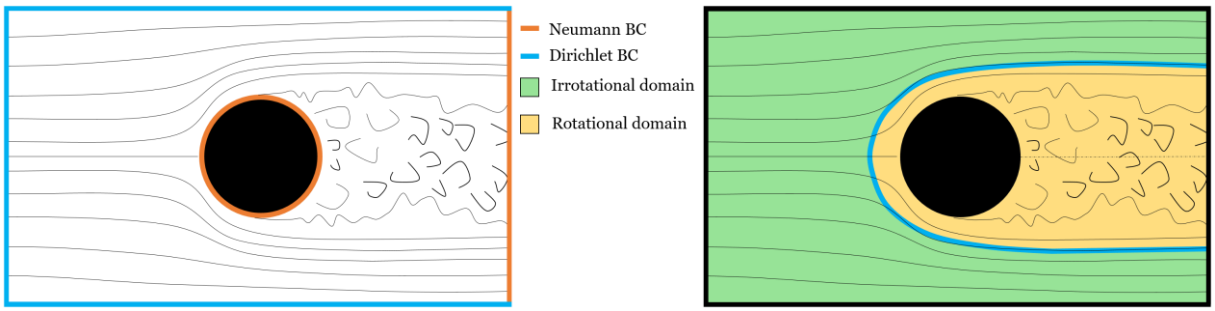

Figure 1: 2D schematic of boundary condition specification to determine the static pressure field by means of the conventional Poisson approach (left), and the proposed multi-model technique (right).

The proposed method aims at mitigating such detrimental effects by partitioning the domain into an irrotational domain, where a point-wise, algebraic computation of the static pressure can be made, and a rotational region where the pressure is obtained through spatial integration. The pressure in the former region provides the necessary Dirichlet boundary conditions for the pressure integration in the rotational domain. The latter region is significantly reduced in size, minimizing the likelihood of error accumulation. In a last step the field pressure is mapped onto the discretized model surface.

2.2.1 Irrotational domain

In the irrotational fluid domain, the most simplifying assumptions can be made. Considering an incompressible flow at moderate to high Reynolds number, then the irrotational flow domain can be modelled by potential flow theory. Hence, Bernoulli's equation applies, with constant total pressure in the entire irrotational domain. For known freestream conditions the relative pressure is given by:

$$\bar{p} - p_\infty = q_\infty - \frac{1}{2}\rho \boldsymbol{u}^2 \tag{2}$$

Where $\boldsymbol{u}$ is the measured time-averaged velocity vector and q_∞ the free-stream dynamic pressure.

2.2.2 Rotational domain

Whereas total pressure in the irrotational domain is considered constant throughout, in the rotational domain constant total pressure may only be assumed along a streamline. Hence, eq. 2 may only be applied along streamlines, however the value of total pressure for any streamline in the rotational domain is not known. Therefore, the static pressure in the rotational domain is obtained through spatial integration of the pressure gradient instead. For a time-averaged, incompressible flow, where viscous terms are negligible, the pressure gradient is given by,

$$\nabla \bar{p} = -\rho(\overline{\boldsymbol{u}} \cdot \nabla)\overline{\boldsymbol{u}} - \rho \nabla \cdot \overline{\boldsymbol{u}'\boldsymbol{u}'} \tag{3}$$

Where the mean velocity $\overline{\boldsymbol{u}}$, its spatial gradient $\nabla\overline{\boldsymbol{u}}$, and the unsteady term $\overline{\boldsymbol{u}'\boldsymbol{u}'}$ are provided by the measurement procedure described in Sec. 2.1. Thus, $\nabla\bar{p}$ can be calculated at all points in the measurement domain. Note that the term related to fluctuations is spatially differentiated by means of second order finite differences on the interior measurement domain and first-order upwind schemes on the domain boundaries.

The integration of the pressure gradient is carried out by a spatial marching process featuring an erosion of the domain from an initial interface with the irrotational domain where a Dirichlet boundary condition is provided. The pressure is assigned for points in the rotational domain featuring a minimum of 8 Dirichlet-type neighbor points (based on a 3×3×3 kernel). For the selected N points, the pressure gradient is integrated from the available neighbors ($\boldsymbol{x}_i$)to the point of interest ($\boldsymbol{x}_e$):

$$\bar{p}(\boldsymbol{x}_e) = \frac{1}{N}\sum_{i=1}^{N}(\bar{p}(\boldsymbol{x}_i) + \Delta\bar{p}_{i-e}) \tag{4}$$

$$\Delta\bar{p}_{i-e} = \frac{1}{2}(\nabla\bar{p}_i + \nabla\bar{p}_e)\cdot(\boldsymbol{x}_e - \boldsymbol{x}_i) \tag{5}$$

At each step of the process, the domain where the static pressure is known is dilated. Conversely, the region of the measurement domain where the static pressure is not integrated yet is eroded. This integration process is sketched in Fig. 2 (left).

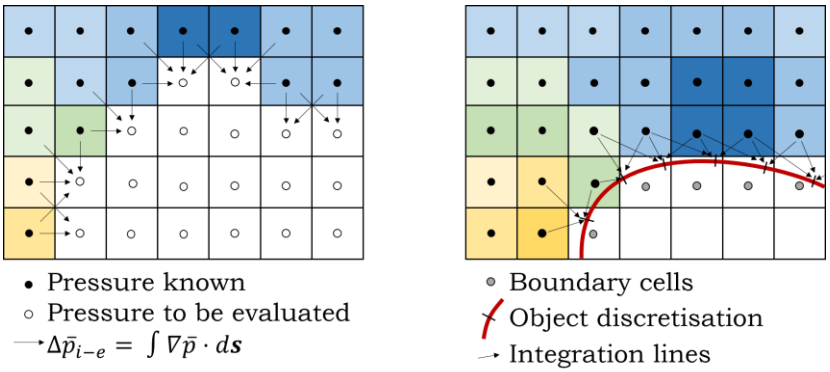

Figure 2: 2D schematic of the pressure integration procedure in the rotational domain (left) and the subsequent line integration to the discretized surface (right).

The algorithm advances until the static pressure is known in all points in the rotational fluid domain, yielding the complete static pressure field in the flow measurement domain. An advantage of the current procedure is that specifying a boundary condition on the object surface is not needed, as illustrated in Fig. 1 (right), which can prove challenging on curved and complex geometries.

2.2.3 Surface pressure

The final step in the proposed method is the evaluation of the surface pressure on the test object. For this work it is assumed that object shape, location and orientation are known with respect to the velocity measurements acquired by the robotic PIV system. This is not a trivial assumption, given the complexity of a volumetric PIV measurement system and a number of reference systems involved with it (Jux et al., 2018a). Furthermore, production tolerances and structural model deformations due to aerodynamic loadings are not accounted for. In this context it is highly recommended to place markers on the test model, which can easily be reconstructed by the tomographic imaging system, thereby assisting in determining the actual position and orientation of the test object to be interfaced with the *flow mesh*. Once the model position and orientation are known, the surface can be discretised at a desired spatial resolution, yielding a surface description by means of a point cloud $\boldsymbol{x}_s$[1].

For each point of the discretized surface $\boldsymbol{x}_s$, the nearest neighbour on the Cartesian flow mesh is located. Any point with a valid pressure value on a 3×3×3 kernel surrounding the nearest neighbor point is then used to compute the static pressure at the surface node in a similar fashion as outlined in eq. 4, namely by integration of the pressure gradient. Here the integral is computed using the gradient value at the pressure nodes. The process is schematically outlined in Fig. 2 (right).

2.3 Domain partitioning

The proposed method relies on different strategies to calculate the static pressure in the flow field. As such, the measurement domain is partitioned into two distinct regions: an irrotational domain where potential flow conditions can be assumed, and a rotational region where less simplifying

[1] In this work a standard .stl type surface description is used where pressure is evaluated at the centres of the triangular mesh faces, but any other type of discrete surface description may be considered.

assumptions can be made. Therefore, a robust and universal identification of the interface between these two domains is important for the success of the pressure evaluation. The domain boundary is defined in three steps which are detailed hereafter.

2.3.1 Minimum object distance

First, a minimum distance to any solid boundary is defined. This is necessary as the detection of rotational flow features requires a minimum kernel of (uncorrelated) velocity vectors in the fluid mesh. Thus, flow rotation may not be correctly identified on the domain boundaries, and in particular in vicinity of solid objects. This motivates the definition of a minimum object distance $|\Delta \boldsymbol{x}_n|$ within which the irrotational flow assumption may not be applied. This distance relates directly to the spatial resolution of the velocity measurement, and a value of two bin-spans l_v has proven to be a conservative choice. Therefore, any point on the fluid mesh which falls inside

$$|\Delta \boldsymbol{x}_n| < 2l_v \tag{6}$$

is considered to be in the rotational fluid domain.

2.3.2 Wake modelling

The second criterion extrapolates the dilated model surface resulting from the previous step in the streamwise direction. The rationale behind this is the fact that any flow passing an obstacle (the test model) at moderate to high Reynolds numbers will feature a wake which convects downstream. Such wake flows are best described by rotational flow. The contour of the dilated surface resulting from eq. 6 is thus extrapolated in the streamwise direction up to the end of the flow domain, creating a volume downstream of the test model within which the presence of rotational flow is assumed.

2.3.3 Turbulence threshold

The third and last criterion is added to cover any other regions of rotational flow which may not be detected by the two criteria above. Imagine e.g. an expanding wake downstream of a wedge, or a more complex flow where the wake flow experiences an advective component out of the streamwise direction. In these examples the geometric detection of the rotational region by the two previous criteria might be incomplete. Therefore, the last criterion assesses the turbulence characteristics to identify any remaining regions of rotational flow. Specifically, the normalised three-dimensional turbulence intensity *TI* is evaluated,

$$TI = \frac{1}{u_\infty}\sqrt{\frac{1}{3}\left(\overline{u'^2} + \overline{v'^2} + \overline{w'^2}\right)} \leq 0.1 \tag{7}$$

and a threshold level of 10% is observed to fulfil the task of identifying turbulent regions with negligible effects due to measurement noise (typically below 3%). The masking of the rotational domain in its three steps is visualized for the case of the sphere in Fig. 3.

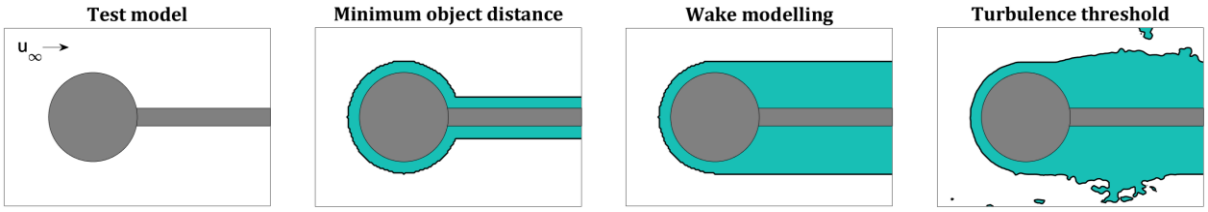

Figure 3: Definition of interface between rotational (green) and irrotational flow domain (white).

3 Experimental apparatus and procedures

The wind tunnel experiments presented in this work are conducted in the Open Jet Facility (OJF) at TU Delft. The closed-circuit wind tunnel features an octagonal 3:1 contraction of the cross section, supplying a 2.85 × 2.85 m² test section. The tunnel is operated at atmospheric conditions, and the turbulence level in the nominal wind speed range is within 1 %.

Helium filled soap bubbles (HFSB, Scarano et al., 2015; Faleiros et al., 2019) are generated by a 10-wing, 200-nozzle rake which is installed in the settling chamber and which is controlled by a *LaVision* fluid supply unit regulating the mass-flow of Helium, soap and air. The HFSB nozzle pitch is 5 cm, with the system spanning a 0.5×1.0 m cross section. Nominally, one nozzle generates 20,000 to 60,000 bubbles of 300 to 550 μm diameter per second. Their specific weight ranges from 0.9 to 1.1 that of the air in the wind tunnel stream.

The robotic PIV system is composed by the *LaVision MiniShaker Aero* (coaxial volumetric velocimeter) and a *Universal Robots UR5* collaborative robotic arm. The CVV probe houses four CMOS imagers in a diamond arrangement along with an optical fiber in its center, transmitting the light generated by a *Quantronix Darwin-Duo Nd-YLF* laser (527 nm, 2 × 25 mJ pulse energy at 1 kHz). The active camera sensors count 640×476 px, with images acquired at 821 Hz through 4 mm lenses.

3.1 Flow around a sphere

A 15 cm diameter sphere is placed in a free stream at 10 m/s. The corresponding Reynolds number $Re_d = 10^5$ lies within the sub-critical flow regime (Achenbach 1972).

Surface pressure taps along 15 azimuthal directions (from -10° to 130°) are integrated in the 3D printed sphere (orifices of 1 mm diameter) in the vertical symmetry plane. An additional tap is placed at 10° in the horizontal symmetry plane, to verify the model alignment with the free stream. The sphere is held from the back with a 1.2 m long, circular supporting sting, as shown in Fig. 4.

Figure 4: Experimental setup in OJF.

During acquisitions the CVV probe is oriented normal to the freestream direction, at approximately 40 cm distance to the sphere center. Each acquisition captures a volume of approximately 15 liter. Streamwise translations of the probe yield flow data up- and downstream of the test model, composing a larger overall measurement volume of roughly 50 liter.

Particle images are recorded in time-resolved mode. A particle moving at nominal free-stream conditions displaces by 12.2 mm between frames, equivalent to 23 px displacement on the camera sensors (at a nominal distance of z = 40 cm). Raw particle images feature a particle image density of approx. 0.01 ppp and they are pre-processed with a high-pass frequency filter (Sciacchitano and Scarano 2014) followed by a mean image subtraction to remove background noise and reflections.

After pre-processing, the images are analysed with the Lagrangian Particle Tracking algorithm Shake-The-Box as implemented in *LaVision - Davis 10*. The data is reduced on a Cartesian mesh by an ensemble averaging procedure as outlined in Sec. 2.1. Spherical cells of 10 mm diameter are considered, yielding a 2.5 mm vector spacing when using 75 % overlap.

3.2 Cyclist study

The measurement data on the full-scale cyclist mannequin is taken from a previous work of the authors, which includes further details on the measurement setup (Jux et al., 2018a). The measurements were conducted with a similar robotic PIV system, in the same wind tunnel. Experiments were conducted at 14 m/s free-stream velocity and ensemble averages are computed as for the sphere flow, in this case with larger bins of 20 mm diameter and a vector spacing of 5 mm.

4 Results and discussion

4.1 Sphere flow assessment

The time-averaged velocity field measured by the robotic PIV system is shown in Fig. 5 (left) by a cross section in the vertical symmetry plane. The corresponding distribution of time-average pressure is illustrated in Fig. 5 (right).

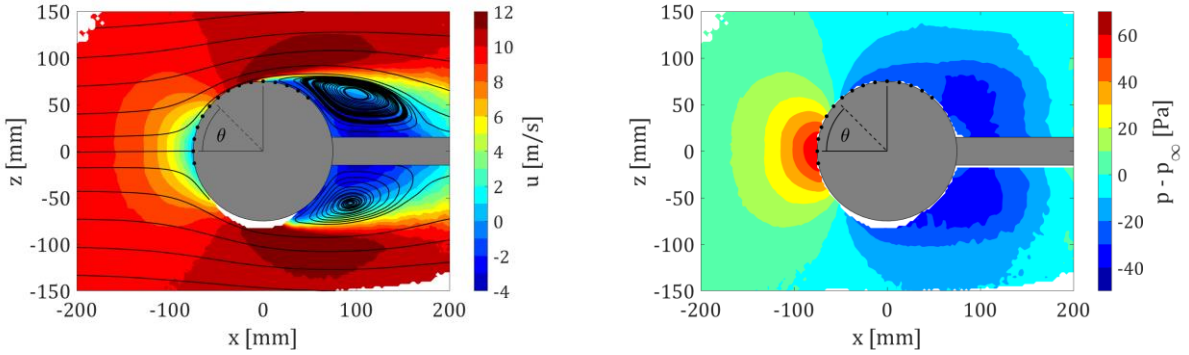

Figure 5: Velocity field in the vertical symmetry plane and corresponding pressure field with locations of wall taps indicated.

The velocity field in Fig. 5 (left) features the stagnation region, corresponded in Fig. 5 (right) with a relative pressure increase of 60 Pa (q_∞ = 60 Pa). The flow accelerates around the object up to approximately θ = 80°. The onset of separation is observed at θ = 90°. In the rear region of the sphere a circulatory motion is established with reverse flow conditions. The pressure distribution exhibits little variation past separation, with an annular region of low pressure (Δp = -30 Pa) in the separated recirculating flow ($\theta \sim 150°$).

The three-dimensional static surface pressure distribution is shown in Fig. 6, along with contours of the streamwise velocity field on orthogonal symmetry planes. From a careful analysis of the 3D surface pressure data, it is observed that the flow field is not fully axis-symmetric, but the flow acceleration in the horizontal plane is more dominant as compared to the acceleration in the *xz*-plane. This translates into a further reduction in surface pressure of up to 4 Pa on the side of the sphere (negative *y*). It is likely that this increased acceleration results from the blockage due to the robotic arm and CVV probe.

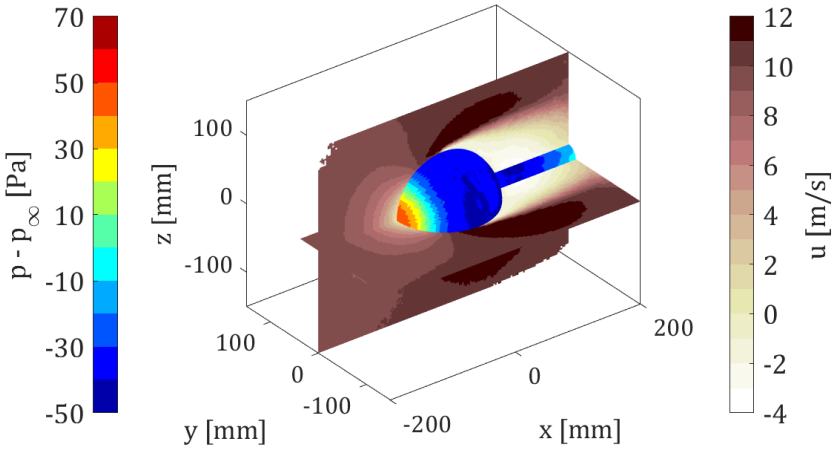

Figure 6: Contours of streamwise velocity in horizontal and vertical symmetry plane along with distribution of static pressure on the discretized test object.

The effect of spatial resolution in the time-averaged velocity measurement on the surface pressure distribution recorded by the robotic PIV system is assessed. For this purpose, the pressure

distribution is compared to the direct measurements obtained from the orifices at the wall. The azimuthal pressure distribution in the *xz*-plane for varying size of the averaging bin (l_v from 10 to 50 mm, at 75% overlap) is plotted in Fig. 7.

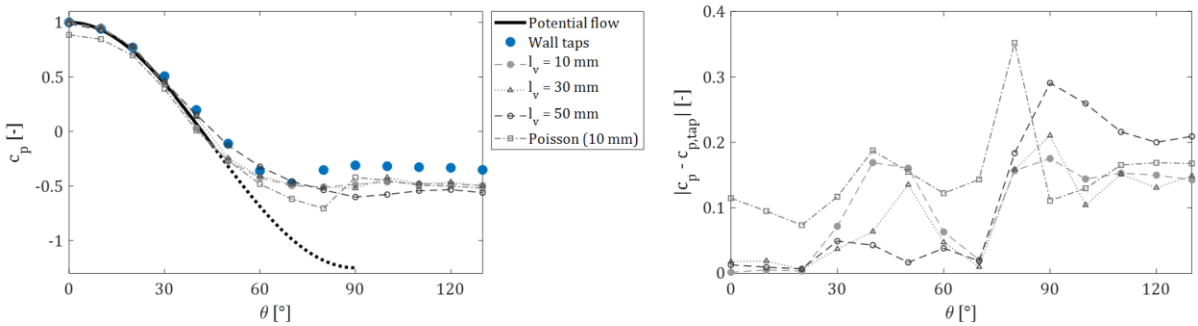

Figure 7: Azimuthal pressure distribution for different spatial resolution levels in the robotic PIV velocity data, compared to the orifice measurements (left), and the relative discrepancy (right).

For the forward part of the sphere, up to $\theta = 30°$, potential flow theory can be considered an accurate approximation of the flow, which is reported (solid black) in Fig. 7 (left) for reference. The direct measurement with orifices is given up to $\theta = 130°$. Figure 7 shows a high degree of correlation between the pressure readings from PIV and the taps for small azimuth angles ($\theta < 30°$), with differences in c_p within 0.02 (1.2 Pa), even at coarsest resolution ($l_v = 50$ mm). As the boundary layer develops, and the azimuthal pressure distribution reaches its maximum gradient ($30° < \theta < 60°$) the static pressure recorded by PIV is lower and closer to the potential flow solution than the orifice recordings. A maximum deviation of 0.17 c_p is observed at 40°. Interestingly, there is no clear effect of spatial resolution visible, except for the largest bin size (50 mm), which flattens the pressure gradient and thus, follows the value returned by the surface orifices more closely. The minimum pressure value at 70° is captured well by the PIV measurement, however, it does not resolve the small recovery (adverse pressure gradient) accordingly, yielding a mismatch of approx. 0.15 c_p (9 Pa) in the separated wake region. Finally, spatial resolution effects only become visible for the 50 mm case ($l_v >$ 0.5 R). One may conclude that for the measurement of the time-average surface pressure distribution, the required spatial resolution corresponds to an interrogation bin not larger than the half the local radius of curvature.

Based on the same velocity data, the surface pressure is also obtained with the Poisson approach, considered to date as the standard practice (van Gent et al. 2017, among others). The results for the finest assessed resolution level ($l_v = 10$ mm) included in Fig. 7 show that solving the Poisson equation systematically underestimates the pressure increase at stagnation by approximately 10%, and returns somewhat higher errors also around separation.

4.2 Flow around full scale cyclist

The aerodynamic study of professional cycling has recently benefited from the use of large-scale PIV to infer the flow-field and even forces acting on the athlete (Spoelstra et al., 2019). Experiments conducted on a full-scale replica of the 2017 time-trial world champion Tom Dumoulin, by robotic PIV have allowed the visualization of the flow in terms of velocity, streamlines and vorticity, helping to understand the main sources of drag and the complex aerodynamic interactions from different segments of the body (Jux et al., 2018a).

The surface pressure distribution is an excellent indicator to identify frontal stagnation areas as well as rear suction regions mostly responsible for increase of drag. To the best of the authors knowledge, there is no likewise (experimental) pressure data on full-scale cyclist models available. Sampling surface pressure from taps is challenging when dealing with a model that is dressed in a racing suit. On a different note, the use of pressure sensitive paint is not reported for the present speed range, mostly due to its limited sensitivity.

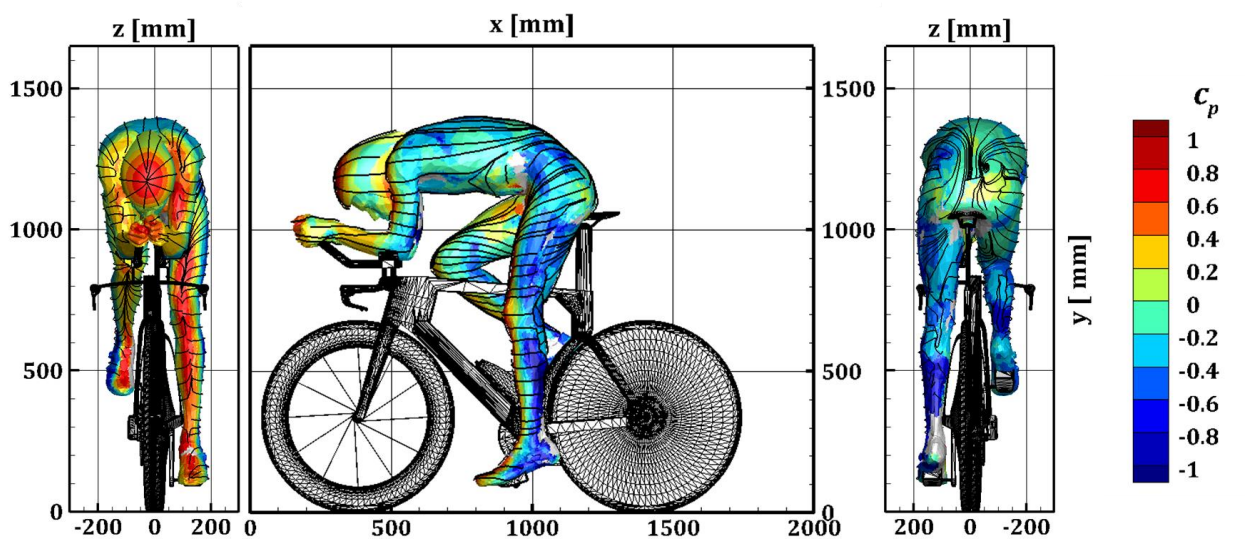

Figure 8: Surface pressure distribution on a full-scale cyclist model at 14 m/s free-stream velocity.

The surface distribution of static pressure on the complete athlete body has been obtained from the database discussed in Jux et al. (2018a). The results are shown in Fig. 8. Clear regions of high pressure are identified on the forward section of the helmet, as well as the rider's fingers and upper arms and his legs, where the flow is decelerating. Asymmetric pressure is observed on the two arms, which is less easily explained than that occurring on the legs, where the stretched left leg faces the flow more bluntly, as compared to the flexed right leg. Regions of low pressure are seen on the side of the legs, feet and arms as a result of rapid acceleration past these curved body parts. Similarly, over the curved shoulders, the back, and the left hip low pressure regions are seen. The former are likely curvature-induced, whereas around the hip, a significant upward flow component creates a local region of suction.

5 Conclusions

A multi-model method for static pressure evaluations based on 3D PTV data is presented. The measurement domain is partitioned into an irrotational part, where pressure is evaluated through Bernoulli's equation, and a rotational domain, where the pressure gradient is spatially integrated in an iterative procedure. In a third step the field pressure is mapped onto the model surface, yielding the static surface pressure distribution.

For the flow around a 15 cm diameter sphere at 10 m/s, the reconstructed surface pressure compares well to reference measurements for small azimuth angles, and in the point of maximum suction. Small mismatches of up to 0.15 c_p are observed in the region of maximum pressure gradient and in the separated wake region instead. It is observed that spatial resolution of the velocity data appears not to be critical as long as the linear dimension of the averaging cell is 50 % smaller than the radius of curvature of the object under investigation.

Applying the proposed method to the flow measurements around a full-scale cyclist model at 14 m/s, yields an unprecedented experimental surface pressure distribution on a human-size object. As the model is partially dressed in fabric, and due to its size, implementation of classical surface pressure probes is infeasible, and the presented PIV based technique provides a valid approach to evaluate the complete 3D surface pressure distribution.

Acknowledgements

The authors acknowledge the insightful discussions held with B.W. van Oudheusden and M. Gerritsma from TU Delft on pressure reconstruction methods.

References

Achenbach E (1972) Experiments on the flow past spheres at very high Reynolds numbers. *Journal of Fluid Mechanics* 54:565-575

Agüera N, Cafiero G, Astarita T, and Discetti S (2016) Ensemble 3D PTV for high resolution turbulent statistics. *Measurement Science and Technology* 27:124011

de Kat R, and van Oudheusden BW (2012) Instantaneous planar pressure determination from PIV in turbulent flow. *Experiments in Fluids* 52:1089-1106

Faleiros DE, Tuinstra M, Sciacchitano A, and Scarano F (2019) Generation and control of helium-filled soap bubbles for PIV. *Experiments in Fluids* 60:40

Ghaemi S, Ragni D, and Scarano F (2012) PIV-based pressure fluctuations in the turbulent boundary layer. *Experiments in fluids* 53:1823-1840

Gregory JW, Asai K, Kameda M, Liu T, and Sullivan JP (2008) A review of pressure-sensitive paint for high-speed and unsteady aerodynamics. In *Proceedings of the Institution of Mechanical Engineers, Part G: Journal of Aerospace Engineering*, 222:249-290

Huhn F, Schanz D, Manovski P, Gesemann S, and Schröder A (2018) Time-resolved large-scale volumetric pressure fields of an impinging jet from dense Lagrangian particle tracking. *Experiments in Fluids* 59:81

Jux C, Sciacchitano A, Schneiders JFG, and Scarano F (2018a) Robotic volumetric PIV of a full-scale cyclist. *Experiments in Fluids* 59:74

Jux C, Sciacchitano A, and Scarano F (2018b) Surface pressure visualization by 3D PTV. In *Proceedings 18th International Symposium on Flow Visualization*. ETH Zurich

Pröbsting S, Scarano F, Bernardini M, and Pirozzoli S (2013) On the estimation of wall pressure coherence using time-resolved tomographic PIV. *Experiments in Fluids* 54:1567

Scarano F, Ghaemi S, Caridi GCA, Bosbach J, Dierksheide U, and Sciacchitano A (2015) On the use of helium-filled soap bubbles for large-scale tomographic PIV in wind tunnel experiments. *Experiments in Fluids* 56:42

Schanz D, Gesemann S, and Schröder A (2016) Shake-The-Box: Lagrangian particle tracking at high particle image densities. *Experiments in Fluids* 57:70

Schneiders JFG, Scarano F, Jux C, and Sciacchitano A (2019) Coaxial volumetric velocimetry. *Measurement Science and Technology* 29:065201

Sciacchitano A, and Scarano F (2014) Elimination of PIV light reflections via a temporal high pass filter. *Measurement Science and Technology* 25:084009

Spoelstra A, de Martino Norante L, Terra W, Sciacchitano A, and Scarano F (2019) On-site cycling drag analysis with the Ring of Fire. *Experiments in Fluids* 60:90

Tagliabue A, Scharnowski S, and Kähler CJ (2017) Surface pressure determination: a comparison between PIV-based methods and PSP measurements. *Journal of Visualization* 20:581-590

Tropea C, Yarin AL, and Foss JF (2007) Springer handbook of experimental fluid mechanics (Vol. 1). Chapter Pressure Measurement Systems, page 179. Springer Science & Business Media

van Gent PL, Michaelis D, van Oudheusden BW, Weiss PÉ, de Kat R, Laskari A, Jeon YJ, David L, Schanz D, Huhn F, Gesemann S, Novara M, McPhaden C, Neeteson NJ, Rival DE, Schneiders JFG, and Schrijer FFJ (2017) Comparative assessment of pressure field reconstructions from particle image velocimetry measurements and Lagrangian particle tracking. *Experiments in Fluids* 58:33

van Oudheusden BW (2013) PIV-based pressure measurement. *Measurement Science and Technology* 24:032001